3D-Printed Biodegradable Microswimmer for Theranostic Cargo Delivery and Release

Author(s):
Ceylan, Hakan; Yasa, Immihan Ceren; Yasa, Öncay; Fatih Tabak, Ahmet; Giltinan, Joshua; Sitti, Metin

Publication date:
2019-03-26

Permanent link:
https://doi.org/10.3929/ethz-b-000657383

Originally published in:
ACS Nano 13(3), https://doi.org/10.1021/acsnano.8b09233

ACS NANO

Cite This: ACS Nano 2019, 13, 3353−3362

www.acsnano.org

ARTICLE

3D-Printed Biodegradable Microswimmer for Theranostic Cargo Delivery and Release

Hakan Ceylan,[†] Immihan Ceren Yasa,[†] Oncay Yasa,[†] Ahmet Fatih Tabak,[†,‡] Joshua Giltinan,[†] and Metin Sitti*[,†]

[†]Physical Intelligence Department, Max Planck Institute for Intelligent Systems, 70569 Stuttgart, Germany

[‡]Mechatronics Engineering Department, Bahcesehir University, 34353 Istanbul, Turkey

Supporting Information

ABSTRACT: **Untethered mobile microrobots have the potential to leverage minimally invasive theranostic functions precisely and efficiently in hard-to-reach, confined, and delicate inner body sites. However, such a complex task requires an integrated design and engineering, where powering, control, environmental sensing, medical functionality, and biodegradability need to be considered altogether. The present study reports a hydrogel-based, magnetically powered and controlled, enzymatically degradable microswimmer, which is responsive to the pathological markers in its microenvironment for theranostic cargo delivery and release tasks. We design a double-helical architecture enabling volumetric cargo loading and swimming capabilities under rotational magnetic fields and a 3D-printed optimized 3D microswimmer (length = 20 μm and diameter = 6 μm) using two-photon polymerization from a magnetic precursor suspension composed from gelatin methacryloyl and biofunctionalized superparamagnetic iron oxide nanoparticles. At normal physiological concentrations, we show that matrix metalloproteinase-2 (MMP-2) enzyme could entirely degrade the microswimmer in 118 h to solubilized nontoxic products. The microswimmer rapidly responds to the pathological concentrations of MMP-2 by swelling and thereby boosting the release of the embedded cargo molecules. In addition to delivery of the drug type of therapeutic cargo molecules completely to the given microenvironment after full degradation, microswimmers can also release other functional cargos. As an example demonstration, anti-ErbB 2 antibody-tagged magnetic nanoparticles are released from the fully degraded microswimmers for targeted labeling of SKBR3 breast cancer cells *in vitro* toward a potential future scenario of medical imaging of remaining cancer tissue sites after a microswimmer-based therapeutic delivery operation.**

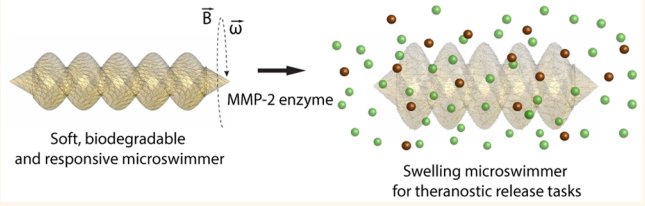

KEYWORDS: *microrobot, 3D printing, drug delivery, hydrogel, gelatin, targeted delivery, biodegradation*

Advancements in interventional technologies have enabled minimally invasive strategies, such as endoscopy or robot-assisted surgery, which have markedly reduced centimeter/decimeter-size incisions of many open surgeries to millimeter-size holes, lowered postoperative patient morbidity, and shortened recovery times.[1,2] The advances and evolution of untethered mobile robots, whose size go down to the level of a single cell, can further leverage minimally invasive medicine by providing a direct access and precise control in deep and delicate body sites, such as the central nervous system, the circulatory system, the fetus, and the eye.[3−8] Recent progress along this line has already resulted in a number of synthetic and biohybrid microrobotic designs with intriguing functionalities toward their use in various pathophysiological environments.[9−14]

Active navigation of highly concentrated therapeutic and diagnostic agents to the site of action could represent a state-of-the-art application of microrobots, considering the limited delivery and distribution efficiencies offered by the systemic routes and local diffusion.[15] By this means, it is possible to minimize the effects of systemic toxicity and increase the overall efficacy of single-dose administration.[16] Autonomous release of multiple types of payloads with programmable kinetics based on the environmental sensing of local cues, such as disease markers, in the living milieu could enable microrobotic therapy and diagnosis in the form of an orderly executed, programmable operation.[17] A conventional robot responds to the changes in its environment by means of its on-board sensors and computational capabilities; however, achieving such capabilities at the smaller dimensions, where such computational capabilities do not exist, remains a major research question.[18] In nature, microorganisms, such as slime molds and bacteria, have evolved to use physical intelligence as the main route of making decisions in complex and evolving conditions.[19] Accordingly, programmed

Received: December 5, 2018
Accepted: February 11, 2019
Published: February 11, 2019

DOI: 10.1021/acsnano.8b09233
ACS Nano 2019, 13, 3353−3362

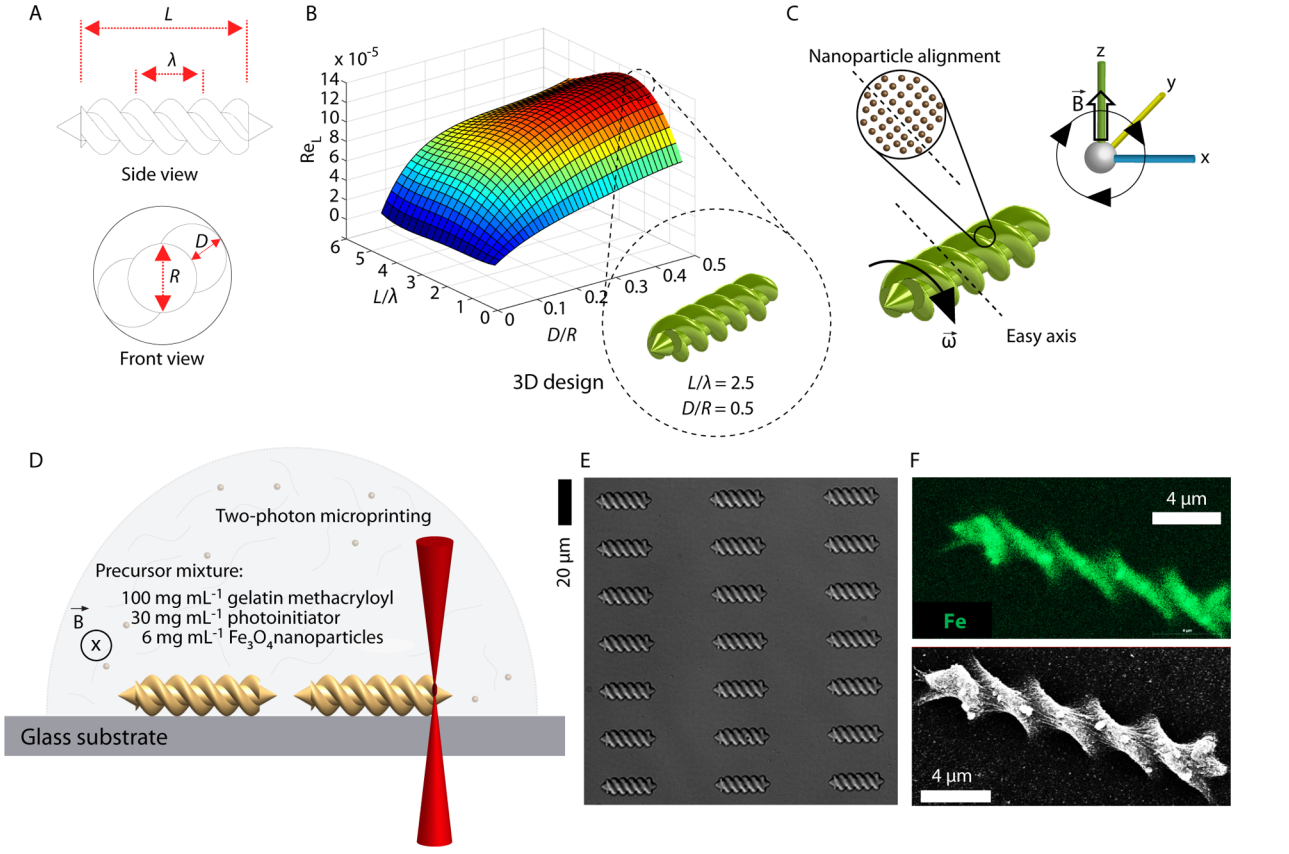

Figure 1. Design and 3D fabrication of biodegradable hydrogel microrobotic swimmers. (A) Empirical design of the double-helical microswimmer. (B) Computational fluid dynamics simulation for Reynolds number with respect to L/λ and D/R ratios, calculated for water at room temperature. The maximum forward swimming velocity was found with $L/\lambda = 2.5$ and $D/R = 0.5$ for the given design space sweep study. (C) Alignment of the magnetic nanoparticles that defines an easy axis normal to the helical axis, thereby allowing rotational motion under rotating magnetic fields. (D) 3D fabrication of the microswimmers using two-photon polymerization. During the fabrication process, a continuous magnetic field was applied to keep the nanoparticles aligned. (E) Optical microscope differential interference contrast (DIC) image of a microswimmer array. (F) Energy-dispersive X-ray spectroscopy mapping of iron confirming the homogeneous embedding of the iron oxide magnetic nanoparticles inside the microswimmer body.

physical and chemical properties of materials can enable a robust design route for making microrobotic systems with the capabilities of motion, sensing, and functioning in dynamic interaction with their local environment.[20,21]

Biodegradability, that is, decomposition over time as a result of the resident biological activity, is a critical aspect of microrobotic design for their safe operation in the living environment. When the prescribed task is accomplished, the safest option for removing the microrobots from the body is to expect their degradation to nontoxic, metabolized products. The use of nondegradable materials can result in serious acute and chronic toxicities, which could require surgical revision, and hence lower the overall desired benefit from the microrobot.[22] As a result, materials that predictably degrade and disappear in a safe manner have become increasingly important for medical applications.[23] Microrobotic systems developed so far have not tackled the issue of biodegradability, so it complicates their clinical use due to possible adverse effects in the body.

In the present study, we report an integrated strategy for the design and fabrication of a hydrogel-based, biodegradable microrobotic swimmer, which accomplishes its tasks of therapeutic and diagnostic release *in vitro* based on the environmental sensing of matrix metalloproteinase 2 (MMP-2) enzyme. In the physiological environment, MMP-2 plays an important role in the tissue remodeling process by degrading various types of collagen that constitute the main fabric of the extracellular matrix. In many cancers, however, tumor cells metastasizing to other tissues use this enzyme to escape from the surrounding matrix, so the local concentration of MMP-2 is elevated.[24,25] The local pathological concentrations of MMP-2 trigger the microswimmer to switch on a boosted drug release pathway by rapidly swelling its hydrogel network. We accomplish the fabrication of magnetically powered, environmentally responsive microswimmers by 3D printing of a nanocomposite magnetic precursor. The precursor comprises iron oxide nanoparticles dispersed in gelatin methacryloyl, a photo-cross-linkable semisynthetic polymer derived from collagen.[26] Gelatin also contains target cleavage sites for MMP-2, thereby appealing as a biodegradable structural material for microrobots.[27] We show that upon the enzymatic breakdown of the microswimmer network, anti-ErbB 2 antibody-tagged magnetic contrast agents are released into the local environment for targeted cell labeling of ErbB 2 overexpressing SKBR3 cancer cells, thereby promising follow-up evaluation strategy of the preceding therapeutic intervention. Altogether, the findings of the present work represent a leap toward *in vivo* mobile microrobots that are capable of sensing, responding to the local microenvironment, and performing specific diagnostic or therapeutic tasks using their smart composite material architectures in physiologically complex environments.

DOI: 10.1021/acsnano.8b09233
ACS Nano 2019, 13, 3353−3362

RESULTS AND DISCUSSION

Design and 3D Printing of Microswimmer Hydrogels.

As the swimmer size goes to microscopic scales, the viscous forces begin to dominate over the inertial forces. As a result, a microswimmer needs to do continuous nonreciprocal motions to break spatial and temporal symmetries to generate a forward thrust.[28] To comply with the same challenge, micro-organisms in nature have evolved elaborate locomotion strategies, such as helical rotation of bacterial flagella, and the beating of paramecium cilia, which have so far inspired many synthetic swimmer designs.[29−34] Inspired by a similar mechanism, the design of our microrobotic swimmer is illustrated in Figure 1. From an empirical point of view, the geometry of the microswimmer comprises a cylindrical core wrapped by a double helix, and the cylinder has cones at both ends. Due to the chirality of the double helix, the rotational motion of the microswimmer is coupled to its translational motion. The structure of the microswimmer primarily involves increasing the volume-to-surface ratio, with the goal of accommodating concentrated therapeutics in its bulk. Previous designs were limited to a simple helix, and the materials used to make them yielded nonporous architectures. As a result, such designs were only for the applications of cargo transport on the swimmer surface, which put significant limitations over the amount of the deliverable cargo and hence the potential efficacy of the microrobotic operations.[32,33,35]

The dimensions of the microswimmer were determined by four parameters: L, λ, D, and R (Figure 1A). The length, L, was fixed to 20.0 μm, and the diameter of the inner cylinder, R, to 3.3 μm, to have a microswimmer on the size order of an average mammalian cell. We then sought to maximize the swimming speed by varying the wavenumber, L/λ, and D/R in a series of computational fluid dynamics simulations and built the equation of motion for the microswimmer (Supporting Information Figures S1−S3; also see supporting Text S1 for a detailed discussion). Swimming motility simulations and experiments were conducted in water at room temperature for a quantitative proof-of-concept study. However, as future *in vivo* translation needs to be conducted in biological fluids, which are non-Newtonian and heterogeneous, application-oriented optimizations will be proposed in future follow-up studies. In water, rotation−translation coupling was observed to lie in an optimum region, yielding the maximum swimming velocity within the confines of the studied design space (Figure 1B and Supporting Information Figure S4). The coupling decreased toward the long and short wavelengths, as, in both cases, the structure geometry lost its chirality and converged to a cylinder and hence lost its ability to generate forward thrust. The coupling also decreased by decreasing the cord radius, D, of the double helix because the interaction surface of the double helix with the surrounding fluid went smaller. Altogether, the dimensionless ratios of $L/\lambda = 2.5$ and $D/R = 0.5$ were evaluated to give the highest swimming speed given the design considerations. Concerning the trajectory stability along a single line, a single helix is expected to swim with lower stability at noninteger wavenumbers, here 2.5, due to the balancing of the hydrodynamic forces throughout the helices.[36] Nevertheless, the design in the form of double helix compensates the trajectory stability. The lateral drift was found to be an order of magnitude higher with the single-helix configuration than that of the double-helix configuration (Supporting Information Figure S5). The wobbling velocity, that is, the lateral angular velocities of the microswimmer with single-helix configuration, was also an order of magnitude higher with the single helix (Supporting Information Figure S6). These simulations showed that the double helix represents an advantageous design scheme in favor of hydrodynamic efficiency and thus power requirements.

The use of magnetic fields is a prominent way of remote powering and control of medical microrobots.[12,37] In contrast to other untethered power transfer alternatives, such as light and chemical fuels, magnetic fields provide a biocompatible source of energy and are able to safely and uniformly penetrate biological tissues.[12] Catalytic microswimmers usually rely on nonbiocompatible fuel sources for propulsion, and those that are moving with biocompatible fuels are unable to move inside biologically relevant ionic media.[38] Powering with light is limited with the penetration depth, safely deliverable light intensity, and the line-of-sight exposure, so it is not applicable to confined and complex *in vivo* environments. Using acoustic fields is a promising method for off-board propulsion and manipulation of microswimmers. However, the functional design of such a microswimmer and its application in a biological setting is currently insufficient and requires future developments.[12] To rotate the double helix, rotating magnetic fields are needed, which then create a torque on the microswimmer through a magnetic axis defined perpendicular to the helical axis. Assuming the external field is invariant, the magnetic force scales with the volume of the magnetic material, that is, L^3, whereas the equivalent force from the magnetic torque scaling with L^2. Thus, swimming by magnetic torque-induced rotation is preferable at smaller scales, less than 100 μm, due to its higher efficiency of thrust generation.[20] We sought to embed superparamagnetic iron oxide nanoparticles in the form of a nanocomposite to impart magnetizability to the microswimmer body. Embedding iron oxide nanoparticles has certain advantages over magnetic surface coating, such as with cobalt or nickel. Cobalt and nickel are considerably toxic to the living environment, whereas iron oxide nanoparticles are mostly regarded as biofriendly.[39] Coating the microswimmer surface would also drastically reduce the availability of the microswimmer bulk for cargo loading and release from the porous hydrogel network. Additionally, biofunctionalization of magnetic nanoparticles provides an opportunity as smart contrast agents for targeted cell labeling toward medical imaging and therapy.[40] In order to create an effective magnetic torque for rotation, introduction of a magnetization axis perpendicular to the helical axis was necessary, which was accomplished by the alignment and entrapment of the magnetic nanoparticles under uniform magnetic field during the fabrication process (Figure 1C,D).[41]

To realize such a design with highly demanding geometrical and compositional aspects, we employed 3D-printing based on two-photon polymerization or direct laser writing (Figure 1D). This fabrication technique relies on the simultaneous absorption of two half-energy photons by the photoinitiator at the tight focal spot of a femtosecond-pulsed infrared laser light. As the two-photon absorption occurs only in a fraction of the focal volume, and the polymer precursor is transparent to the infrared laser wavelength (*i.e.*, 780 nm), spatiotemporal control of the two-photon absorption enables highly complex 3D computer-aided designs with submicron features. For the printing, we prepared a nanocomposite hydrogel precursor containing 100 mg mL^{-1} gelatin methacryloyl, 30 mg mL^{-1} photoinitiator, and 6 mg mL^{-1} iron oxide nanoparticles, which we ensured to be compatible with two-photon polymerization (Supporting Information Figures S7 and S8). The structural fidelity of the

DOI: 10.1021/acsnano.8b09233
ACS Nano 2019, 13, 3353−3362

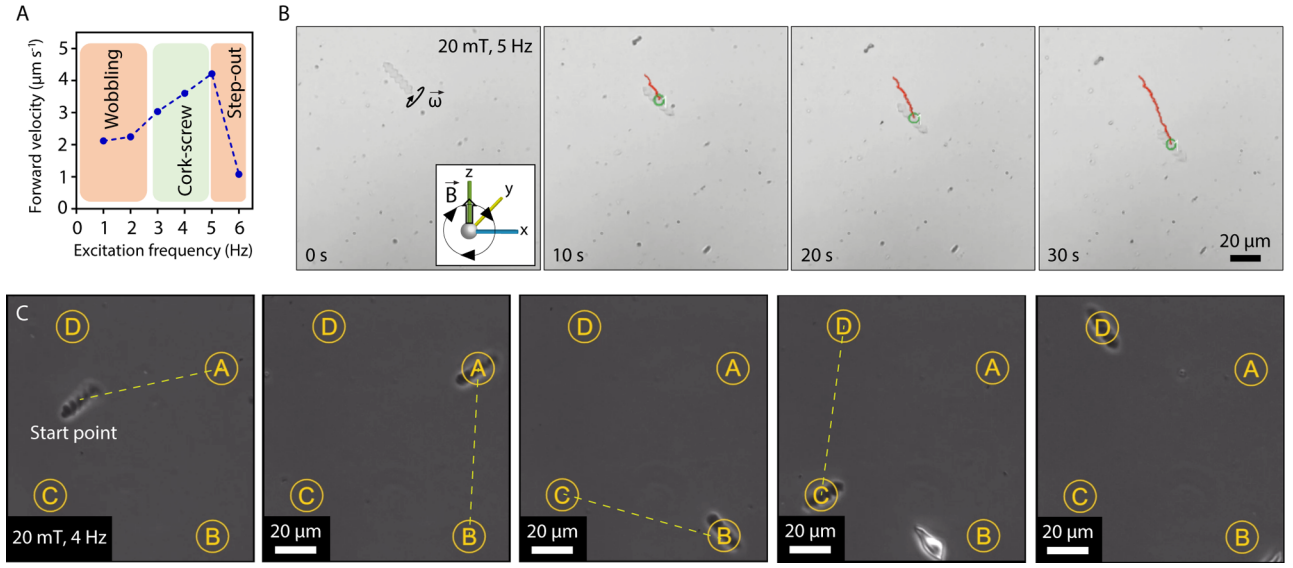

Figure 2. Swimming trajectory of a double-helix microswimmer under a rotating magnetic field. (A) Step-out frequency of the microswimmers containing 6 mg mL^{-1} iron oxide nanoparticles was found to be around 6 Hz. (B) Image sequence of the hydrogel microswimmer actuated under a rotating magnetic field with the magnetic field strength and excitation frequency being 20 mT and 5 Hz, respectively. The average velocity of the microswimmers was found to be 3.36 ± 0.71 μm s^{-1}. (C) Magnetic steering control of the microswimmer. A microswimmer is given the task of reaching each checkpoint from A to D.

resulting microswimmers was in agreement with the design, and we did not observe undesired shrinkage or swelling in the polymerization and development steps (Figure 1E). Energy-dispersive X-ray analysis proved homogeneous distribution of the iron oxide nanoparticles inside the microswimmer (Figure 1F and Figure S9).

The total amount of magnetic nanoparticles loaded in the mesh network of the microswimmer body is critical for the magnitude of magnetization and hence the swimming speed. Decreasing the amount will result in lower step-out frequencies, thereby reducing the achievable translational thrust with the design. Therefore, we aimed to maximize the volume fraction of the magnetic nanoparticles in the precursor suspension. Nevertheless, increased concentrations of nanoparticles from 0.1 to 10 mg mL^{-1} narrowed down the effective laser energy density range for both low and high laser intensities (Figure S10). At lower laser intensities, the aggregates of nanoparticles at higher nanoparticle concentrations physically blocked the propagation of the polymerization because there are fewer chains generated to complete the assigned laser trajectories, and insufficiently linked structures lowered the structural quality. At higher laser intensities, nanoparticle aggregates strongly interacted with the laser light, resulting in local heating, bubble generation, and structural damage. This problem could be potentially circumvented with iron oxide nanoparticles that have better colloidal stability, and hence they have lesser tendency for aggregation at higher concentrations. In the current nanoparticle design, microscopic aggregates were evident during polymerization above 6 mg mL^{-1} iron oxide nanoparticle concentration. In this regard, this threshold concentration was used in the rest of the microswimmer preparations, as they were homogeneously dispersed in the solution without any particle aggregation or agglomeration (Figure S8). Additionally, the two-photon lithography method does not reach temperatures that would affect the magnetic properties of the iron oxide nanoparticles.

Mobility of Microswimmers. For magnetic mobilization, we utilized a custom six-coil electromagnetic setup to create rotating magnetic fields that exert a computer-controlled magnetic torque on the microswimmer's long axis (Figures S3 and S11). We determined the step-out frequency of the microswimmers loaded with 6 mg mL^{-1} iron oxide nanoparticles by increasing input frequency at every 10 s starting from 1 to 6 Hz with 1 Hz step size at 20 mT. The swimming velocity increased linearly with increasing excitation frequency (Figure 2A and Supporting Video S1). The microswimmers exhibited predominantly wobbling behavior in the frequency range of 1−3 Hz. The cork-screw motion was observed in the range of 3−5 Hz. The step-out frequency of the microswimmers was 6 Hz. We characterized the long-distance trajectory of the microswimmers by actuating them at 5 Hz, just below their step-out frequency, to determine their average swimming speed (3.36 ± 0.71 μm s^{-1}) (Figure 2B and Supporting Video S2). Temporally constant rotating fields in the work space allow navigation of microswimmers as small teams (Supporting Video S2). Magnetic steering control of the biodegradable microswimmers was shown with a given the task of reaching checkpoints from A to D (Figure 2C and Supporting Video S2).

Biodegradability with MMP-2. Matrix metalloproteinases operate in the extracellular environment and play an important role in tissue remodeling by degrading various extracellular matrix components. These enzymes could, therefore, represent an appealing target for the proteolytic degradation of our microswimmers once they have completed their prescribed tasks. In a healthy individual, MMP-2 is reportedly present at various concentrations, yet typically in the range of 140−200 ng mL^{-1}, depending on the type of tissue that is expressed.[24,25] At an unrealistically high concentration of MMP-2 (*i.e.*, 100 μg mL^{-1}), we observed that the microswimmers were entirely degraded within an hour *in vitro* at 37 °C (Supporting Video S3). The complete degradation time was a function of the initial MMP-2 concentration (Figure 3A,B). At more realistic concentrations, such as 4 μg mL^{-1}, it took around 5 h for complete degradation, 67 h at 0.500 μg mL^{-1}, and 118 h at 0.125 μg mL^{-1}, that is, the physiological level. The degradation

DOI: 10.1021/acsnano.8b09233
ACS Nano 2019, 13, 3353−3362

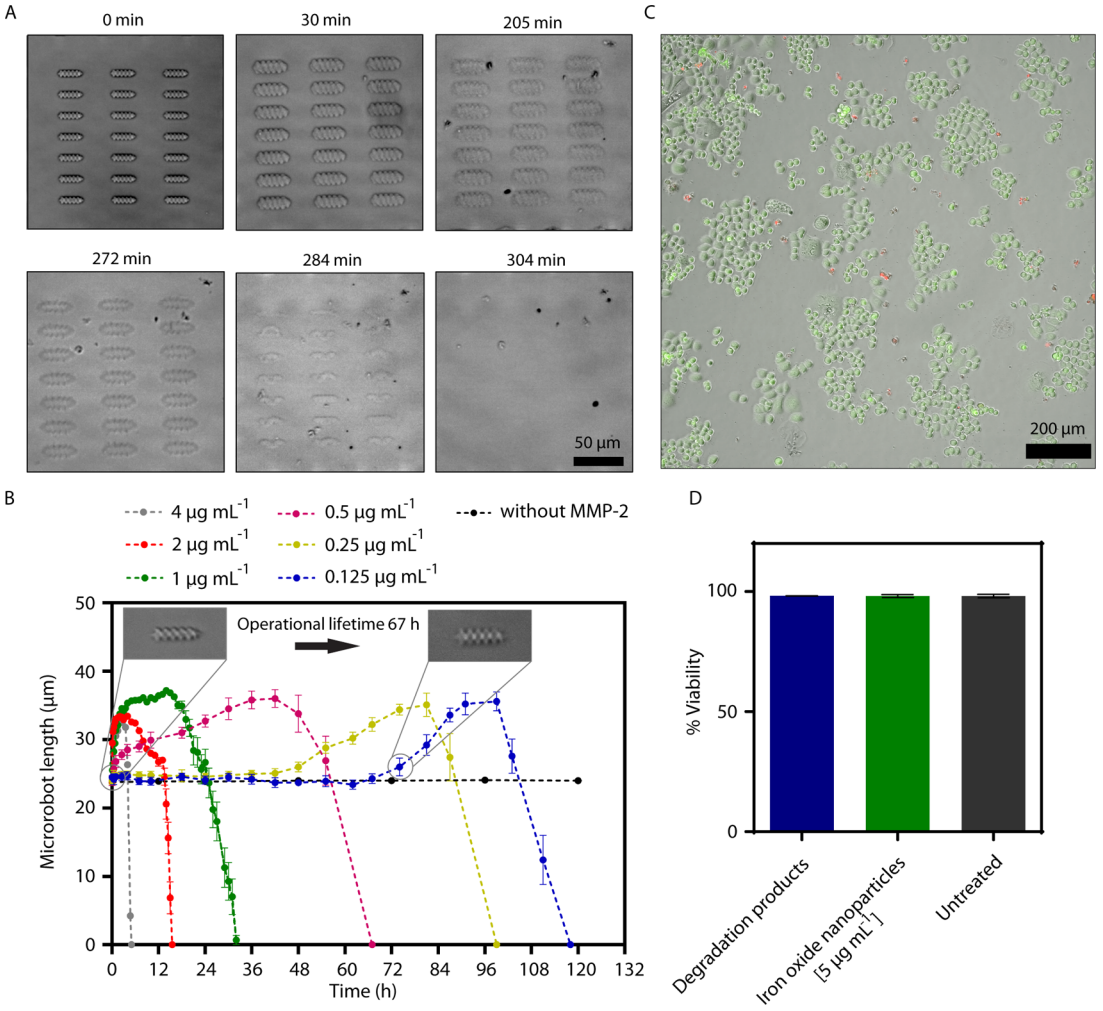

Figure 3. Biodegradation of the hydrogel microswimmers by the MMP-2 enzyme. (A) DIC images of a degrading microswimmer array in the presence of 4 μg mL^{-1} enzyme. Degradation starts with the rapid swell of the microswimmers followed by the collapse of the entire network. (B) Enzymatic degradation of the microswimmers. At the physiological level, MMP-2 degrades the microswimmers within 118 h. Enzymatic susceptibility introduces a concept of operational lifetime, defined as the time period that microswimmer preserves its original morphology for proper navigation. The operational lifetime is a function of the enzyme concentration in the microenvironment. Data are presented as mean ± standard deviation. (C) Live (green) and dead (red) SKBR3 breast cancer cells treated with the degradation products of the microswimmers. (D) Quantitative analysis of the acute toxicity induced by the degradation products of the microswimmers in comparison with 5 μg mL^{-1} iron oxide nanoparticles and untreated cells. Data are presented as mean ± standard deviation.

kinetics of microswimmers should be more closely investigated for a target application at a specific tissue, considering all the tissue-specific proteases and other local conditions. Very recently, salt-based erosion of inorganic microswimmers was shown for the route of microswimmer degradation in the living environment.[42] The present study presents a microrobotic swimmer that is completely removed by a physiologically relevant enzymatic process, which leaves no detectable toxic residues behind (Figure 3C,D). Although we did not observe an acute toxicity with the SKBR3 cell line, even in the presence of high iron oxide nanoparticle concentrations, given the potential long-term toxicity risks raised by the use of nanoparticles should be taken into account in the line of the current literature.[39] We anticipate that the degradation time could be further extended by introducing nondegradable methacryloyl polymers, such as poly(ethylene glycol), in the microswimmer network, so that the density of the enzyme recognition sites would be lowered.

A one-way shape memory response of the microswimmers to the enzyme emerged in the degradation process. Following the introduction of MMP-2, we observed concentration-dependent swelling of the microswimmer body more than 3-fold its initial volume, followed by the collapse of the entire hydrogel network (Figure 3B). The swelling of the microswimmers indicates that MMP-2 enzymes could diffuse into the microswimmers and started the hydrolysis of the polymer chains uniformly across the microswimmer body. In the swelling phase, the enlarged pores were filled by the water molecules that diffused into the polymer network at a rate faster than the hydrolysis of the polymer chains near the microswimmer surface. This relationship suggests that the observed phenomenon is homogeneous or bulk erosion.[23] In bulk degradation, water continues to diffuse until it saturates the entire network. As the rate of water diffusion exceeds the rate of the bond cleavage reaction, uniform swelling is observed long before the collapse of the network.[43] At this phase, the concentration of the hydrolyzable bonds is high. As the degradation continues, the polymer segments start dissolving inside water, and the loss of mass becomes observable throughout the material in a homogeneous manner. This is observable in the microscopy images of the microswimmers shown in Figure 3A. At 4 μg mL^{-1} MMP-2 concentration, the

DOI: 10.1021/acsnano.8b09233
ACS Nano 2019, 13, 3353−3362

double helices of the microswimmers remain visible over the first 205 min, until which the microswimmers already swelled about 3.5-fold by volume. At 272 min, surface erosion becomes clearly detectable, followed by rapid and total degradation of the microswimmers. Taking into account the morphological change of the microswimmers, a therapeutic time window appears for the microrobotic tasks to be carried out in a controlled way. The operational lifetime ends before the complete degradation, when the microswimmers start swelling (a volumetric expansion above 2% was considered as the threshold value) because the microswimmers would then lose their ability to navigate due to significant loss of the structural chirality. The operational lifetime of the microswimmers in the physiological environment is around 67 h, whereas the complete degradation time is 118 h. As a result, the task of a biodegradable microrobot concerning its navigation and localization should be accomplished within the operational lifetime (Figure 3B).

Boosted Drug Release. A major compositional fraction of hydrogels is water, typically accounting for more than 90% by mass. Highly porous hydrogel networks can thus very effectively sequester high amounts of therapeutic and diagnostic cargo types, which can then be released in response to various input signals with controllable spatial and temporal schemes.[44,45] As noted previously, overexpression of matrix metalloproteinases is associated with almost any cancer types because degradation of the matrix promotes tumor-cell growth, migration, invasion, metastasis, and angiogenesis.[46] For example, the concentration of MMP-2 above 200 ng mL^{-1} in the serum was associated with colorectal cancer patients, whereas the quantitative amounts are largely unknown for other cancer types.[25] MMP-2 could thus represent a valuable biomarker for the disease state of the tissue to be sensed and acted upon by the microswimmers. In this regard, the rapid swelling of the microswimmers as an initial response at the elevated concentrations of MMP-2 could serve as a switch for accelerated drug release. As a hydrogel swells, the mesh size increases, and the entrapped drug is released. Because the mesh size is correlated with the extent of swelling, the initial MMP-2 concentration could regulate the overall release kinetics. To this end, we first studied the relationship between the swelling kinetics and the initial enzyme concentration (Figure 4A). At 0.125 μg mL^{-1} MMP-2 concentration, around the physiological level, swelling response was not evident in the first 30 min. At 0.250 μg mL^{-1}, the swelling began to occur after 20 min following the introduction of the enzyme. At 0.5 and 1 μg mL^{-1}, the swelling started as soon as the enzyme was introduced. A more detailed investigation of the MMP-2-mediated swelling showed that the microswimmers exhibit high sensitivity to the pathological MMP-2 concentrations, whereas they retain their original size under physiological conditions, which underpins the stimuli-responsive autonomous behavior of the microswimmers (Figure S12a). The ionic strength of the solution and the proteinaceous content of the environment have also varying impact on the rate of the MMP-2-mediated swelling of the microswimmers at 37 °C (Figure S12b). A typical limitation of swelling-controlled drug delivery with bulk hydrogels is their slow responsiveness due to the slow influx of water into the network. However, as our microswimmer is small, and so is the diffusion length, and highly porous, the response was fast and robust. As a result, the volume of the microswimmers increased by ca. 60% within the first 30 min in the presence of 1 μg mL^{-1} MMP-2. This volumetric expansion considerably accelerated (more than 20%) the model drug−analogue dye release as an initial response to high enzyme concentration (Figure 4B and

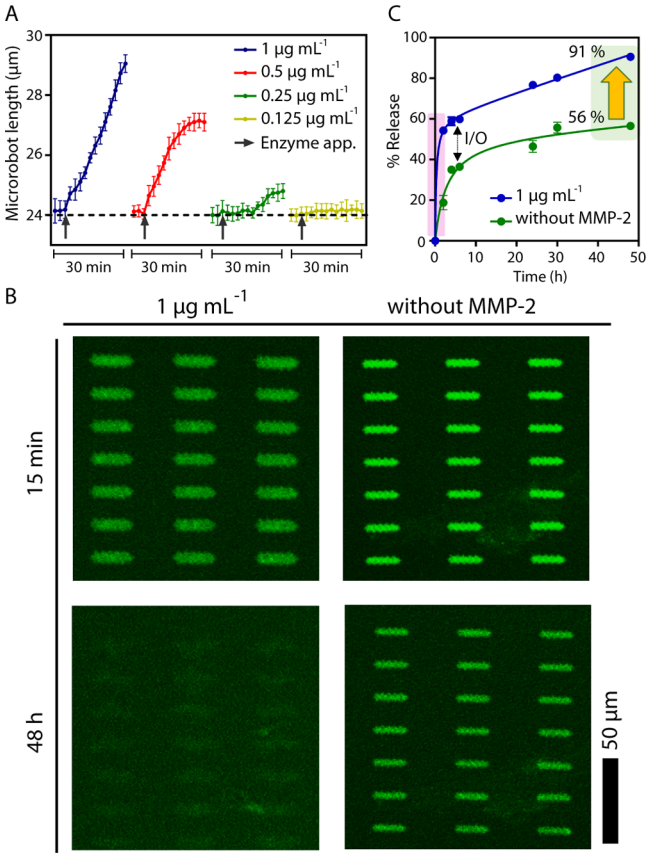

Figure 4. Enzymatically controlled drug release from the hydrogel microswimmers. (A) Elevated concentrations of MMP-2 cause rapid swelling of the microswimmer body, thereby acting as a switch for accelerated drug release. Data are presented as mean ± standard deviation. (B) At 1 μg mL^{-1} MMP-2 concentration, accelerated drug release in the first few hours (the pale pink region) is attributed to swelling-mediated mesh size increase. At the end of 2 days, almost all the payload is released from the degraded microswimmers, whereas half of the content is retained in the nondegraded one, which severely reduces the bioavailability of a significant portion of the drug to be delivered (pale green region). Data as presented with mean ± standard deviation. (C) Epifluorescence images of microswimmers with loaded dextran-FITC cargo used as a model macromolecular drug equivalent. Enhanced drug bioavailability is evidenced by the enzymatic degradation of the network, which releases its entire content.

Figure S13). Control over the drug release kinetics from the microswimmers in response to pathological cues in the microenvironment is particularly valuable for effective and proportional engagement with the disease. Biodegradation is highly valuable in order to be able to fully utilize the drug cargo in the hydrogel network. Without degradation, almost the half of the payload remains inside the network and hence is a sign of poor bioavailability. On the other hand, network degradation increases the bioavailability of the drug payload by releasing all of its content from the microswimmers (Figure 4B,C).

Targeted Cell Labeling. The enzymatic collapse of the hydrogel network further releases the magnetic nanoparticles that are used to provide the magnetic torque for locomotion. We envision that targeted labeling of tumor cells with these locally released magnetic contrast agents could later enable follow-up evaluation of the preceding therapeutic release. For this, we modified the nanoparticle surface to display anti-ErbB 2

DOI: 10.1021/acsnano.8b09233
ACS Nano 2019, 13, 3353−3362

antibody for targeting ErbB 2 receptors, which is overexpressed in the breast cancer cell line SKBR3. For the ease of analysis *in vitro*, the nanoparticles were also modified with fluorophores (Figure 5A). The antibody-tagged nanoparticles were embedded inside the microswimmers similarly to their nonmodified counterparts (Figure 5B). The modification of the nanoparticles does not impair the overall swimming performance of the microswimmers. We explored the cell labeling performance of the magnetic nanoparticles released from the microswimmers *via* MMP-2-mediated degradation. Following the degradation of the microswimmers, the functional nanoparticles released into the environment labeled 39.3% of SKBR3 cells for the detection with fluorescence-activated cell sorting method (Figure 5C and Figure S14). On the other hand, only 9.5% of the cell population was labeled without the surface modification of the nanoparticles, which shows a small degree of nonspecific interaction existed between the cell and nanoparticles, as well (Figure 5D).

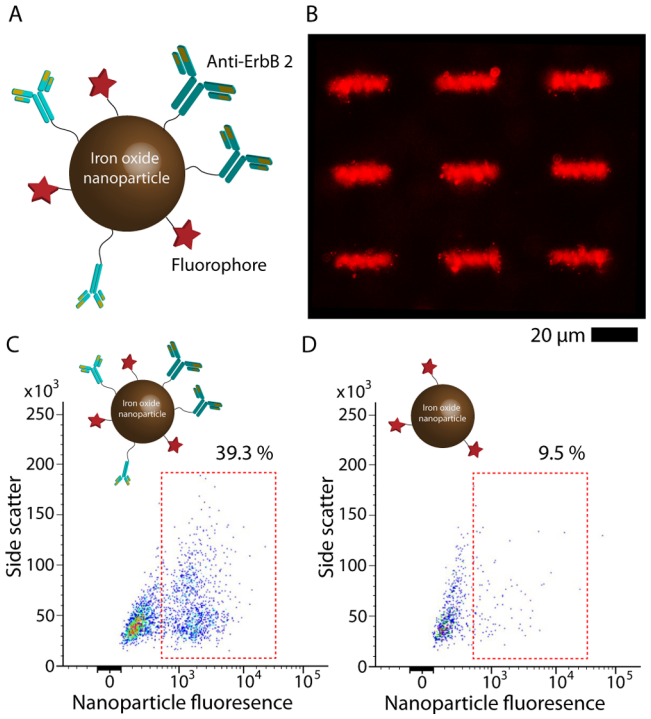

Figure 5. Targeted cell labeling with the magnetic nanoparticles released from collapsed microswimmers toward diagnostic *in vivo* imaging. (A) Design of superparamagnetic iron oxide nanoparticles of 50 nm size functionalized with a fluorophore and anti-ErbB 2 antibody for targeted labeling of ErbB 2-overexpressing breast cancer SKBR3 cells. (B) Epifluorescence image of microswimmers embedded with the nanoparticles. (C) Targeted labeling of SKBR3 with the anti-ErbB 2 modified magnetic nanoparticles released upon the MMP-2-mediated degradation of the microswimmers. In the absence of anti-ErbB 2, the nanoparticles fail to target SKBR3 cells (D).

The combination of therapeutic and diagnostic release capabilities in a soft biodegradable microswimmer could enable semiautonomous and minimally invasive microrobotic operations, where the impact of the therapeutic intervention could be monitored by locating the remaining target cells with the magnetic contrast agents. In a potential theranostic application, the microswimmers could be injected to the vicinity of a tumor (Figure 6). From there, they could be remotely controlled through microtracks by the external magnetic fields for precise navigation, steering, and localization to the tumor with minimum possible damage to the surrounding sensitive tissues. Although the mobility of the microswimmers is externally controlled, therapeutic intervention *via* controlled cargo release is achieved autonomously based on the pathological signal input at the tumor microenvironment. The present work reports the MMP-2 enzyme that triggers boosted cargo release at pathological concentrations, whereas physiological enzyme concentration remains below the detection limit. The MMP-2 concentration is also able to modulate the swelling kinetics, which ensures that there might be adequate drug dose delivered and sustained at extended time intervals (Figure S12a). Spatially strategic localization of multiple microswimmers can tune the locally delivered doses of therapeutics based on the local intensities of the pathological signals. The significant volumetric expansion of the hydrogel matrix could also be turned into an advantage to blockade vessels for tumor chemoembolization. For such and other scenarios, a large team of microswimmers would be required, and control strategies to this end are being developed.[47,48] Long-distance navigation of the microswimmers across distant body sites, that is, on the order of tens of centimeters, remains a grand challenge, as this would require multiple tissue barriers that need to be passed and reliable steering in the bloodstream with overwhelmingly high flow rates. Overcoming tissue barriers requires engineering of the swimmers with higher functional capabilities acting in concert with the environmental signals. Our group and others are in parallel exploring strategies to enable a higher degree of freedom for the operations of microrobotic swimmers in complex live environments.[49,50] Additionally, during any *in vivo* medical operation, the microswimmers need to be monitored with medical imaging techniques, such as magnetic resonance imaging and fluoroscopy due to the presence of iron oxide nanoparticles as contrast agents for magnetic fields and X-rays, respectively.[7,42]

CONCLUSION

As the clinical interest of robotic devices is shifting to the development of small, autonomous, or remotely controlled systems, challenges remain regarding material biocompatibility, biodegradability, and execution of functional tasks in a programmed way. An ideal material solution should convey the idea of short-term inertness in the body, whereas a microrobot should be degradable with the lowest possible waste profile in the long term. Here, we designed, explored, and characterized *in vitro* a hydrogel-based biodegradable helical microswimmer remotely controlled by rotating magnetic fields. Owing to their emergent physical properties and capability to protect labile drugs from degradation, hydrogels could be programmed for various physiochemical interactions with the encapsulated drugs to control drug release. The use of a biopolymer derivative, gelatin methacryloyl, to make microrobots can enable making patient-specific microrobots using their own biomaterials. Such a personalized strategy could largely circumvent potential concerns of immunogenicity. Over the past decade, a variety of microswimmers has been proposed; however, here we complementarily concentrated on the sensing and response to changes in the pathological microenvironment, such as a disease marker enzyme, MMP-2, which triggered the microswimmer to accelerate the therapeutic cargo release at the tumor site. Active and targeted delivery of multifunctional cargo types, such as drugs, imaging agents, genes, and RNA, are the major objectives of microrobotic operations in order to make a

DOI: 10.1021/acsnano.8b09233
ACS Nano 2019, 13, 3353−3362

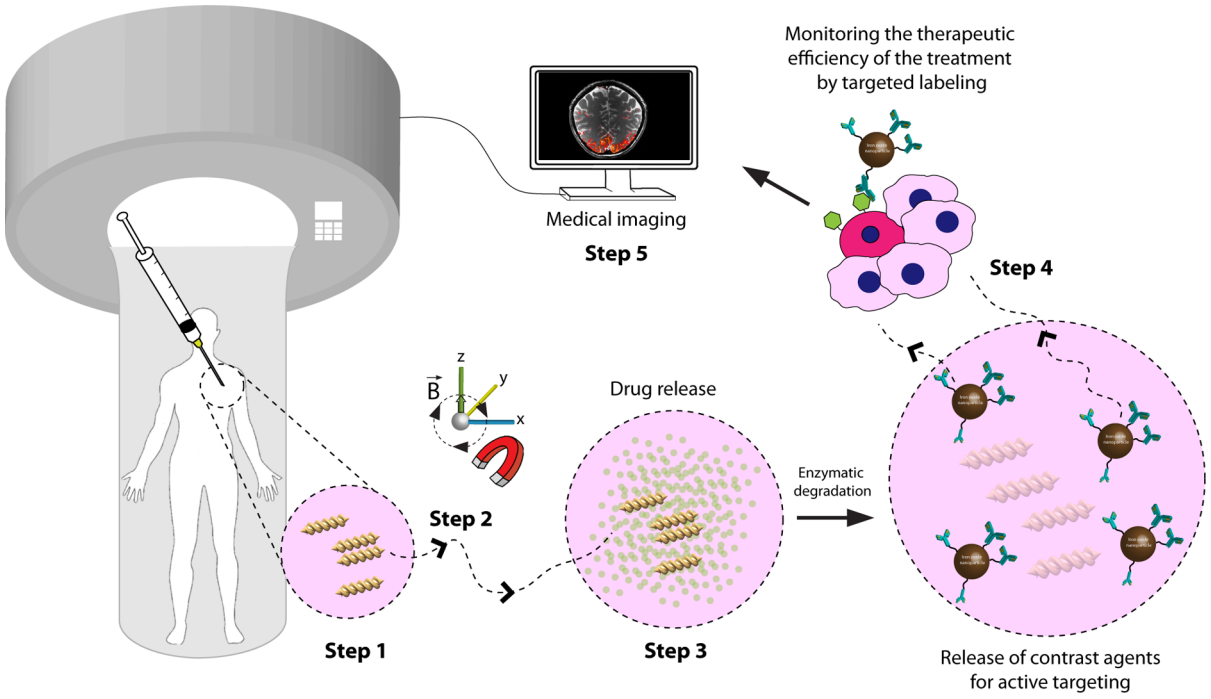

Figure 6. Envisioned theranostic application scenario of the 3D-printed, biodegradable microrobotic swimmers. Step 1: Injection of the microswimmers to the vicinity of a tumor site. Step 2: Active navigation and precise localization of the microswimmers at the site of medical intervention by means of remote magnetic powering and steering. Step 3: Therapeutic intervention with controlled cargo release based on the pathological signal input at the tumor microenvironment. The present work reports the MMP-2 enzyme that triggers boosted cargo release at pathological concentrations, whereas physiological enzyme concentration goes undetected. The degradation of microswimmers further enables full therapeutic cargo bioavailability. Step 4: Complete biodegradation enables both the safe removal of the microswimmers and the release of diagnostic contrast agents. Step 5: Antibody-modified magnetic contrast agents diffuse around to label the untreated tissue sites. The labeled sites could thus be monitored in a minimally invasive manner to assess the therapeutic efficiency of the treatment, and to identify the intervention sites in the next round.

theranostic impact in the near future. Although such capabilities could enable high impact applications in targeted delivery, microsurgery, tissue engineering, and regenerative medicine, in the longer term, they could also provide treatment strategies for genetic diseases by single-cell-level proteins or nucleic acid delivery and roaming the body for disease prediction and prevention.

MATERIALS AND METHODS

Preparation of a 3D-Printable Superparamagnetic Magnetic Precursor. Gelatin methacryloyl (100 mg mL^{-1}), lithium phenyl-(2,4,6-trimethylbenzoyl) phosphinate (30 mg mL^{-1}), iron oxide nanoparticles (6 mg mL^{-1}), coated with poly(ethylene glycol) amine, of 50 nm hydrodynamic size (Chemicell GmbH, Germany), were mixed in ultrapure water with vortex mixing and ultrasound sonication. The resulting suspension was dropped on a glass slide, on which the fabrication was carried out. Commercially available direct laser writing system (Photonic Professional, Nanoscribe GmbH, Germany) with a 63× oil-immersion objective (NA 1.4) was used for 3D printing of the microrobots *via* two-photon polymerization. Laser power and galvanometric mirror *x*- and *y*-scanning speeds were optimized for printing as 23.5 mW and 3.0 × 10^5 μm s^{-1}, respectively (Supporting Information Figure S10). The overall microprinting rate was measured to be 10 s for a single microrobot. DIC images were taken with Nikon Eclipse Ti-E inverted microscope. Energy-dispersive X-ray spectroscopy (EDS) measurements were made with a Zeiss Gemini 500 scanning electron microscope equipped with Quantax EDS (Bruker).

Microswimmers printed on glass substrate, and kept at 4 °C refrigerator overnight in water, were equilibrated to room temperature prior to recombinant human MMP-2 (Sigma-Aldrich) addition at various concentrations (Figure 3B and Figure 4A). Time-lapse images were taken using a Nikon Eclipse Ti-E inverted microscope at 20× magnification in the DIC mode. The enzyme solutions incubated with the microswimmers were replenished every 12 h in order to minimize the impact of enzymatic deactivation at long time periods. For analysis, the length of the microswimmers (21 microswimmers for each time frame) was measured using Nikon NIS AR Element analysis software.

In order to investigate the toxicity of the microswimmer degradation products, the viability of ErbB 2-overexpressing SKBR3 cells (DSMZ, Germany) was tested by live/dead cell imaging kit (Invitrogen) after 24 h of treatment with degradation products (from 2349 microswimmers degraded in 2 μg mL^{-1} MMP-2) and bare nanoparticles, according to manufacturer's instructions. SKBR3 cells were cultured in McCoy's 5a modified medium supplemented with 10% FBS, penicillin (50 UI mL^{-1}), and streptomycin (50 μg mL^{-1}). Cells were grown at 37 °C and 5% CO_2 in a humidified environment and subcultured before confluence using trypsin/EDTA. Cells with no treatment were used as a control. Live and dead cells were observed under fluorescent microscope using FITC and TRITC filters.

Drug Release Assay. Microswimmers printed on glass substrate were loaded with a drug-equivalent macromolecule, dextran-FITC (M_w 10 000 Da, Sigma-Aldrich), by immersing the glass into 1 mM dextran-FITC-containing aqueous solution overnight at 4 °C. The microswimmers were equilibrated to room temperate and washed with copious amount of water for 10 min before the drug release measurements. Drug release from microswimmers was analyzed using a spinning disc (Yokogawa, Japan) confocal microscope (Nikon Eclipse Ti-E). Before the experiment, a separate array of microswimmer was exposed to the varying intensities of laser light and exposure times in order to eliminate the bleaching effect (Figure S13). Confocal fluorescence images were then acquired from the actual release samples every hour for a period of 12 h, then every 6 h by the end of 48 h. MMP-2 was added only in the beginning, and no enzyme replenishment was done afterward. Fluorescence intensities over 21 microswimmers were

DOI: 10.1021/acsnano.8b09233
ACS Nano 2019, 13, 3353−3362

measured using Nikon software. Background fluorescence was subtracted from the measured values.

Cellular Viability and Targeted Cell Labeling. For cell labeling assay, SKBR3 cells at 1×10^5 cells/mL density were incubated with microswimmer degradation products (from 2349 microswimmers degraded in 2 μg mL^{-1} MMP-2) in HEPES buffered saline for 1 h at 37 °C. Nanoparticles without anti-ErbB 2 antibody served as the negative control. After incubation, cells were centrifuged, washed, and resuspended in buffer and analyzed by flow cytometry (BD FACSMelody). Untreated SKBR3 cells were used to set the gates, and a total of 5000 events was acquired for each analysis after gating on singlets (Figure S14).

Statistical Analysis. All experiments were independently repeated at least four times. In each repeat, at least 21 individual microswimmers were counted. The error bars represent ± standard deviation. The statistical analyses were done with one-way analysis of variance (ANOVA). A P value higher than 0.05 was considered statistically significant. The quantitative results represent the overall average of independent and technical replicas.

ASSOCIATED CONTENT

Supporting Information

The Supporting Information is available free of charge on the ACS Publications website at DOI: 10.1021/acsnano.8b09233.

Hydrodynamic optimization of the microswimmer body; materials and methods; building the magnetic coil setup; Figures S1−S14 and Table S1 (PDF)

Video S1: Determination of the step-out frequency of the biodegradable microswimmers (MPG)

Video S2: Long-distance trajectory of the biodegradable microswimmers, microswimmer teams, and magnetic steering control (MPG)

Video S3: Enzymatic degradation of the microswimmers by MMP-2 (MPG)

AUTHOR INFORMATION

Corresponding Author

*E-mail: sitti@is.mpg.de.

ORCID

Hakan Ceylan: 0000-0002-5928-5675
Immihan Ceren Yasa: 0000-0002-5013-7246
Oncay Yasa: 0000-0002-0282-6127
Ahmet Fatih Tabak: 0000-0003-3311-6942
Metin Sitti: 0000-0001-8249-3854

Author Contributions

H.C. and M.S. conceived and oversaw the study. H.C. developed the empirical microswimmer design, and A.F.T. optimized the microswimmer with quantitative analyses and CFD simulations. H.C. developed the additive manufacturing process. J.G. and A.F.T. developed the magnetic actuation setup. O.Y. performed the swimming tests and the analysis. H.C. performed the biodegradations tests. I.C.Y. performed all cell culture works. H.C. and C.Y. performed the drug release and cell targeting tests. All authors contributed to the writing of the manuscript.

Notes

A part of this study was posted to BioRxiv.[51]

The authors declare no competing financial interest.

ACKNOWLEDGMENTS

The authors acknowledge funding from the Max Planck Society and the Max Planck ETH Center for Learning Systems.

REFERENCES

(1) Darzi, A.; Munz, Y. The Impact of Minimally Invasive Surgical Techniques. *Annu. Rev. Med.* **2004**, *55*, 223−237.

(2) Davies, B. Robotic Surgery − A Personal View of the Past, Present and Future. *Int. J. Adv. Robot. Syst.* **2015**, *12*, 54.

(3) Sitti, M. Miniature Devices: Voyage of the Microrobots. *Nature* **2009**, *458*, 1121−1122.

(4) Erkoc, P.; Yasa, I. C.; Ceylan, H.; Yasa, O.; Alapan, Y.; Sitti, M. Mobile Microrobots for Active Therapeutic Delivery. *Adv. Ther.* **2019**, *2*, 1800064.

(5) Sitti, M.; Ceylan, H.; Hu, W.; Giltinan, J.; Turan, M.; Yim, S.; Diller, E. Biomedical Applications of Untethered Mobile Milli/Microrobots. *Proc. IEEE* **2015**, *103*, 205−224.

(6) Fusco, S.; Ullrich, F.; Pokki, J.; Chatzipirpiridis, G.; Özkale, B.; Sivaraman, K. M.; Ergeneman, O.; Pané, S.; Nelson, B. Microrobots: A New Era in Ocular Drug Delivery. *Expert Opin. Drug Delivery* **2014**, *11*, 1815−1826.

(7) Martel, S. Beyond Imaging: Macro- and Microscale Medical Robots Actuated by Clinical MRI Scanners. *Sci. Robot.* **2017**, *2*, eaam8119.

(8) Wang, X.; Luo, M.; Wu, H.; Zhang, Z.; Liu, J.; Xu, Z.; Johnson, W.; Sun, Y. A Three-dimensional Magnetic Tweezer System for Intra-embryonic Navigation and Measurement. *IEEE Trans. Robot.* **2018**, *34*, 240−247.

(9) Felfoul, O.; Houle, D.; Lafleur, M.; Gaboury, L.; Tabrizian, M.; Kaou, N.; Atkin, M.; Vuong, T.; Batist, G.; Beauchemin, N.; Radzioch, D.; Martel, S.; et al. Magneto-aerotactic Bacteria Deliver Drug-containing Nanoliposomes to Tumour Hypoxic Regions. *Nat. Nanotechnol.* **2016**, *11*, 941−947.

(10) de Ávila, B. E.-F.; Angsantikul, P.; Li, J.; Angel Lopez-Ramirez, M.; Ramírez-Herrera, D. E.; Thamphiwatana, S.; Chen, C.; Delezuk, J.; Samakapiruk, R.; Ramez, V.; Obonyo, M.; Zhang, L.; Wang, J. Micromotor-Enabled Active Drug Delivery for *in vivo* Treatment of Stomach Infection. *Nat. Commun.* **2017**, *8*, 272.

(11) Hu, W.; Lum, G. Z.; Mastrangeli, M.; Sitti, M. Small-scale Soft-bodied Robot with Multimodal Locomotion. *Nature* **2018**, *554*, 81−85.

(12) Ceylan, H.; Giltinan, J.; Kozielski, K.; Sitti, M. Mobile Microrobots for Bioengineering Applications. *Lab Chip* **2017**, *17*, 1705−1724.

(13) Chen, C.; Karshalev, E.; Li, J.; Soto, F.; Castillo, R.; Campos, I.; Mou, F.; Guan, J.; Wang, J. Transient Micromotors That Disappear When No Longer Needed. *ACS Nano* **2016**, *10*, 10389−10396.

(14) Sattayasamitsathit, S.; Kou, H.; Gao, W.; Thavarajah, W.; Kaufmann, K.; Zhang, L.; Wang, J. Fully Loaded Micromotors for Combinatorial Delivery and Autonomous Release of Cargoes. *Small* **2014**, *10*, 2830−2833.

(15) Li, J.; Esteban-Fernández de Ávila, B.; Gao, W.; Zhang, L.; Wang, J. Micro/Nanorobots for Biomedicine: Delivery, Surgery, Sensing, and Detoxification. *Sci. Robot* **2017**, *2*, eaam6431.

(16) Cohen, J. Clinical Trials: IL-12 Deaths: Explanation and a Puzzle. *Science* **1995**, *270*, 908a.

(17) Such, G. K.; Yan, Y.; Johnston, A. P. R.; Gunawan, S. T.; Caruso, F. Interfacing Materials Science and Biology for Drug Carrier Design. *Adv. Mater.* **2015**, *27*, 2278−2297.

(18) Siciliano, B.; Khatib, O. *Springer Handbook of Robotics*, 2nd ed.; Springer-Verlag: Berlin, 2016.

(19) Reid, C. R.; MacDonald, H.; Mann, R. P.; Marshall, J. A. R.; Latty, T.; Garnier, S. Decision-making Without a Brain: How an Amoeboid Organism Solves the Two-armed Bandit. *J. R. Soc., Interface* **2016**, *13*, 20160030.

(20) Sitti, M. *Mobile Microrobotics*, 1st ed.; MIT Press, 2017.

(21) Ceylan, H.; Yasa, I. C.; Sitti, M. 3D Chemical Patterning of Micromaterials for Encoded Functionality. *Adv. Mater.* **2017**, *29*, 1605072.

(22) Ulery, B. D.; Nair, L. S.; Laurencin, C. T. Biomedical Applications of Biodegradable Polymers. *J. Polym. Sci., Part B: Polym. Phys.* **2011**, *49*, 832−864.

DOI: 10.1021/acsnano.8b09233
ACS Nano 2019, 13, 3353−3362

(23) Lyu, S.; Sparer, R.; Untereker, D. Analytical Solutions to Mathematical Models of the Surface and Bulk Erosion of Solid Polymers. *J. Polym. Sci., Part B: Polym. Phys.* **2005**, *43*, 383−397.
(24) Thrailkill, K.; Cockrell, G.; Simpson, P.; Moreau, C.; Fowlkes, J.; Bunn, R. C. Physiological Matrix Metalloproteinase (MMP) Concentrations: Comparison of Serum and Plasma Specimen. *Clin. Chem. Lab. Med.* **2006**, *44*, 503−504.
(25) Groblewska, M.; Mroczko, B.; Gryko, M.; Pryczynicz, A.; Guzińska-Ustymowicz, K.; Kędra, B.; Kemona, A.; Szmitkowski, M. Serum Levels and Tissue Expression of Matrix Metalloproteinase 2 (MMP-2) and Tissue Inhibitor of Metalloproteinases 2 (TIMP-2) in Colorectal Cancer Patients. *Tumor Biol.* **2014**, *35*, 3793−3802.
(26) Yue, K.; Trujillo-de Santiago, G.; Alvarez, M. M.; Tamayol, A.; Annabi, N.; Khademhosseini, A. Synthesis, Properties, and Biomedical Applications of Gelatin Methacryloyl (GelMA) Hydrogels. *Biomaterials* **2015**, *73*, 254−271.
(27) Toth, M.; Sohail, A.; Fridman, R. Assessment of Gelatinases (MMP-2 and MMp-9) by Gelatin Zymography. In *Metastasis Research Protocols*; Dwek, M., Brooks, S. A., Schumacher, U., Eds.; Humana Press: Totowa, NJ, 2012; pp 121−135.
(28) Purcell, E. M. Life at Low Reynolds Number. *Am. J. Phys.* **1977**, *45*, 3−11.
(29) Bell, D. J.; Leutenegger, S.; Hammar, K. M.; Dong, L. X.; Nelson, B. J. Flagella-like Propulsion for Microrobots Using a Magnetic Nanocoil and Rotating Electromagnetic Field. *IEEE Int. Conf. Robot. Autom.* **2007**, 1128−1133.
(30) Ghosh, A.; Fischer, P. Controlled Propulsion of Artificial Magnetic Nanostructured Propellers. *Nano Lett.* **2009**, *9*, 2243−2245.
(31) Tottori, S.; Zhang, L.; Qiu, F.; Krawczyk, K. K.; Franco-Obregón, A.; Nelson, B. J. Magnetic Helical Micromachines: Fabrication, Controlled Swimming, and Cargo Transport. *Adv. Mater.* **2012**, *24*, 811−816.
(32) Venugopalan, P. L.; Sai, R.; Chandorkar, Y.; Basu, B.; Shivashankar, S.; Ghosh, A. Conformal Cytocompatible Ferrite Coatings Facilitate the Realization of a Nanovoyager in Human Blood. *Nano Lett.* **2014**, *14*, 1968−1975.
(33) Qiu, F.; Fujita, S.; Mhanna, R.; Zhang, L.; Simona, B. R.; Nelson, B. J. Magnetic Helical Microswimmers Functionalized with Lipoplexes for Targeted Gene Delivery. *Adv. Funct. Mater.* **2015**, *25*, 1666−1671.
(34) Lum, G. Z.; Ye, Z.; Dong, X.; Marvi, H.; Erin, O.; Hu, W.; Sitti, M. Shape-programmable Magnetic Soft Matter. *Proc. Natl. Acad. Sci. U. S. A.* **2016**, *113*, E6007−E6015.
(35) Walker, D.; Käsdorf, B. T.; Jeong, H.-H.; Lieleg, O.; Fischer, P. Enzymatically Active Biomimetic Micropropellers for the Penetration of Mucin Gels. *Sci. Adv.* **2015**, *1*, e1500501.
(36) Tabak, A. F.; Yesilyurt, S. Computationally-validated Surrogate Models for Optimal Geometric Design of Bio-inspired Swimming Robots: Helical Swimmers. *Comput. Fluids* **2014**, *99*, 190−198.
(37) Qiu, F.; Nelson, B. J. Magnetic Helical Micro- and Nanorobots: Toward their Biomedical Applications. *Engineering* **2015**, *1*, 021−026.
(38) Patiño, T.; Arqué, X.; Mestre, R.; Palacios, L.; Sánchez, S. Fundamental Aspects of Enzyme-Powered Micro- and Nanoswimmers. *Acc. Chem. Res.* **2018**, *51*, 2662−2671.
(39) Mahmoudi, M.; Hofmann, H.; Rothen-Rutishauser, B.; Petri-Fink, A. Assessing the *in vitro* and *in vivo* Toxicity of Superparamagnetic Iron Oxide Nanoparticles. *Chem. Rev.* **2012**, *112*, 2323−2338.
(40) Peng, X.-H.; Qian, X.; Mao, H.; Wang, A. Y.; Chen, Z.; Nie, S.; Shin, D. M. Targeted Magnetic Iron Oxide Nanoparticles for Tumor Imaging and Therapy. *Int. J. Nanomed.* **2008**, *3*, 311−321.
(41) Kim, J.; Chung, S. E.; Choi, S.-E.; Lee, H.; Kim, H. J.; Kwon, S. Programming Magnetic Anisotropy in Polymeric Microactuators. *Nat. Mater.* **2011**, *10*, 747−752.
(42) Yan, X.; Zhou, Q.; Vincent, M.; Deng, Y.; Yu, J.; Xu, J.; Xu, T.; Tang, T.; Bian, L.; Wang, Y.-X. J.; Kostarelos, K.; Zhang, L. Multifunctional Biohybrid Magnetite Microrobots for Imaging-guided Therapy. *Sci. Robot.* **2017**, *2*, eaaq1155.
(43) Laycock, B.; Nikolić, M.; Colwell, J. M.; Gauthier, E.; Halley, P.; Bottle, S.; George, G. Lifetime Prediction of Biodegradable Polymers. *Prog. Polym. Sci.* **2017**, *71*, 144−189.
(44) Calvert, P. Hydrogels for Soft Machines. *Adv. Mater.* **2009**, *21*, 743−756.
(45) Li, J.; Mooney, D. J. Designing Hydrogels for Controlled Drug Delivery. *Nat. Rev. Mater.* **2016**, *1*, 16071.
(46) Egeblad, M.; Werb, Z. New Functions for the Matrix Metalloproteinases in Cancer Progression. *Nat. Rev. Cancer* **2002**, *2*, 161−174.
(47) Servant, A.; Qiu, F.; Mazza, M.; Kostarelos, K.; Nelson, B. J. Controlled *in vivo* Swimming of a Swarm of Bacteria-like Microrobotic Flagella. *Adv. Mater.* **2015**, *27*, 2981−2988.
(48) Rahmer, J.; Stehning, C.; Gleich, B. Spatially Selective Remote Magnetic Actuation of Identical Helical Micromachines. *Sci. Robot.* **2017**, *2*, eaal2845.
(49) Mostaghaci, B.; Yasa, O.; Zhuang, J.; Sitti, M. Bioadhesive Bacterial Microswimmers for Targeted Drug Delivery in the Urinary and Gastrointestinal Tracts. *Adv. Sci.* **2017**, *4*, 1700058.
(50) Walker, D.; Käsdorf, B. T.; Jeong, H.-H.; Lieleg, O.; Fischer, P. Enzymatically Active Biomimetic Micropropellers for the Penetration of Mucin Gels. *Sci. Adv.* **2015**, *1*, e1500501.
(51) Ceylan, H.; Yasa, I. C.; Yasa, O.; Tabak, A. F.; Giltinan, J.; Sitti, M. *3D-Printed Biodegradable Microswimmer for Drug Delivery and Targeted Cell Labeling*. *BioRxiv* **2018**, DOI: 10.1101/379024.

DOI: 10.1021/acsnano.8b09233
ACS Nano 2019, 13, 3353−3362